Acta Crystallographica Section F
Structural Biology and Crystallization Communications
ISSN 1744-3091

Structure of the catalytic domain of the *Tannerella forsythia* matrix metallopeptidase karilysin in complex with a tetrapeptidic inhibitor

Tibisay Guevara,[a] Miroslaw Ksiazek,[b] Peter Durand Skottrup,[c]‡ Núria Cerdà-Costa,[a] Sergio Trillo-Muyo,[a] Iñaki de Diego,[a] Erik Riise,[c] Jan Potempa[b,d] and F. Xavier Gomis-Rüth[a]*

[a]Proteolysis Lab, Molecular Biology Institute of Barcelona, Spanish Research Council CSIC, Barcelona Science Park, c/Baldiri Reixac 15-21, 08028 Barcelona, Catalonia, Spain, [b]Department of Microbiology, Faculty of Biochemistry, Biophysics and Biotechnology, Jagiellonian University, Ul. Gronostajowa 7, 30-387 Kraków, Poland, [c]Biomolecular Interaction Group, Department of Drug Design and Pharmacology, Faculty of Health and Medical Sciences, University of Copenhagen, Copenhagen, Denmark, and [d]Oral Health and Systemic Diseases Research Group, University of Louisville School of Dentistry, Louisville, Kentucky, USA

‡ Present address: DAKO Denmark, an Agilent Technologies Company, Produktionsvej 42, DK-2600 Glostrup, Denmark.

Correspondence e-mail: xgrcri@ibmb.csic.es

Received 9 January 2013
Accepted 18 March 2013

PDB Reference: Kly18–SWFP complex, 4in9

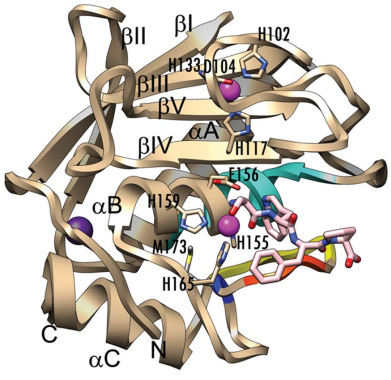

Karilysin is the only metallopeptidase identified as a virulence factor in the odontopathogen *Tannerella forsythia* owing to its deleterious effect on the host immune response during bacterial infection. The very close structural and sequence-based similarity of its catalytic domain (Kly18) to matrix metalloproteinases suggests that karilysin was acquired by horizontal gene transfer from an animal host. Previous studies by phage display identified peptides with the consensus sequence *X*WFP*XXX*GGG (single-letter amino-acid codes; *X* represents any residue) as karilysin inhibitors with low-micromolar binding affinities. Subsequent refinement revealed that inhibition comparable to that of longer peptides could be achieved using the tetrapeptide SWFP. To analyze its binding, the high-resolution crystal structure of the complex between Kly18 and SWFP was determined and it was found that the peptide binds to the primed side of the active-site cleft in a substrate-like manner. The catalytic zinc ion is clamped by the α-amino group and the carbonyl O atom of the serine, thus distantly mimicking the general manner of binding of hydroxamate inhibitors to metallopeptidases and contributing, together with three zinc-binding histidines from the protein scaffold, to an octahedral-minus-one metal-coordination sphere. The tryptophan side chain penetrates the deep partially water-filled specificity pocket of Kly18. Together with previous serendipitous product complexes of Kly18, the present results provide the structural determinants of inhibition of karilysin and open the field for the design of novel inhibitory strategies aimed at the treatment of human periodontal disease based on a peptidic hit molecule.

1. Introduction

Bacterial infection is responsible for periodontitis, an inflammatory gum disease that affects 10–15% of adults worldwide (Petersen & Ogawa, 2005). In the most severe forms of the disease, which may result in tooth loss, three bacterial species are found which form the 'red complex': *Porphyromonas gingivalis*, *Treponema denticola* and *Tannerella forsythia* (Socransky *et al.*, 1998; Rôças *et al.*, 2001). Infection entails the secretion of virulence factors that contribute to disease progression, and among such factors are proteolytic enzymes. In *T. forsythia*, proteolytic virulence factors have been found to include the cysteine proteinase PrtH, the trypsin-like serine proteinase BspA and, most recently, the metallopeptidase (MP) karilysin, which is responsible for the degradation of bactericidal peptides and the inactivation of host complement (Sharma, 2010; Karim *et al.*, 2010; Cerdà-Costa *et al.*, 2011; Koziel *et al.*, 2010; Jusko *et al.*, 2012). Karilysin and *Bacillus anthracis* MmpZ (Pomerantsev *et al.*, 2011) are the only members of the matrix metalloproteinase (MMP) family within the metzincin clan of MPs (Gomis-Rüth, 2003, 2009) characterized from bacteria, which strongly suggests that these proteins arose from eukaryotic-to-prokaryotic horizontal gene transfer, resulting in xenology (Cerdà-Costa *et al.*, 2011). Recently, the three-dimensional structure of the catalytic MMP-like domain of karilysin, Kly18, was analyzed with and without magnesium (Cerdà-Costa *et al.*, 2011), as alkaline-earth metals had been reported to be

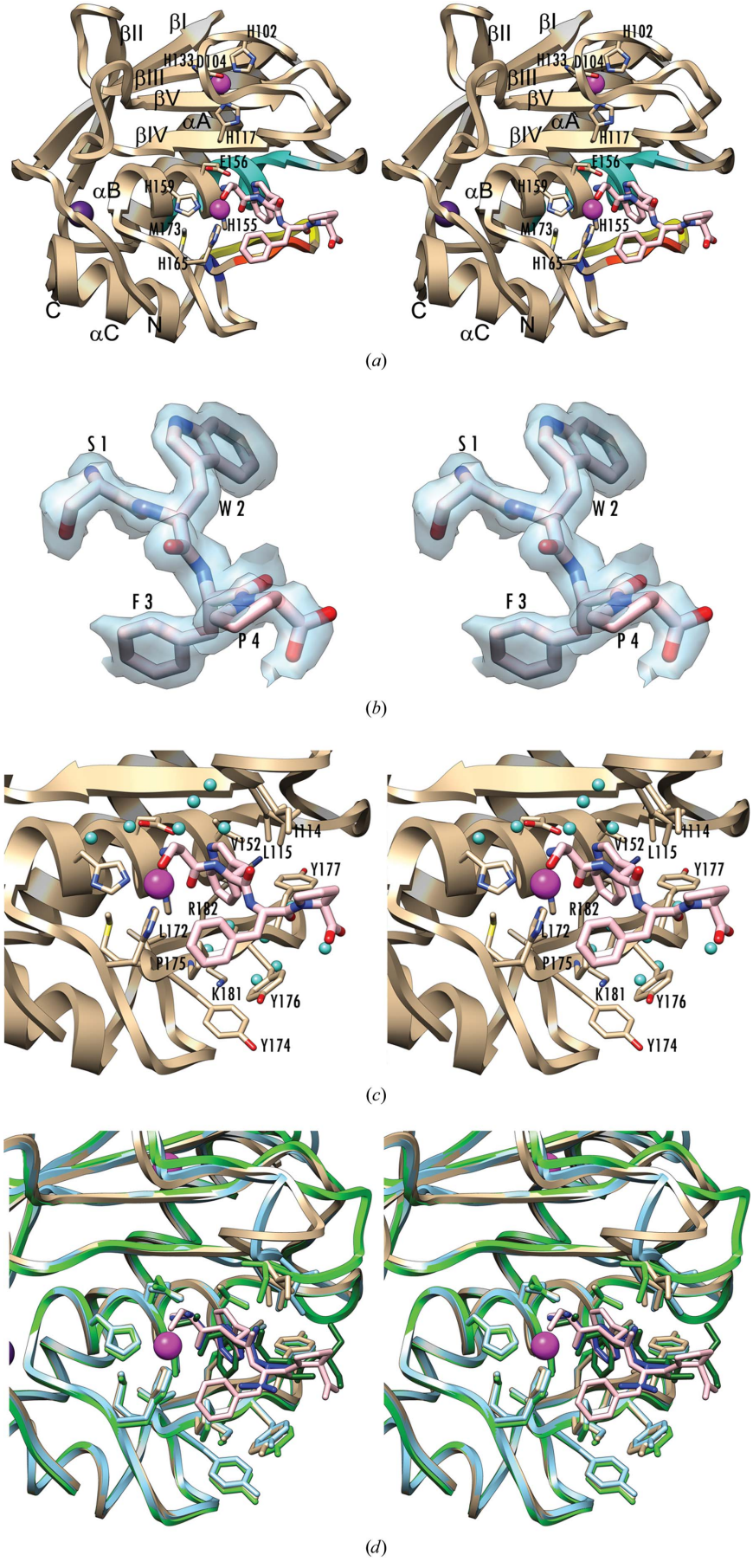

required for activity (Karim *et al.*, 2010). In addition, initial inhibitory studies of karilysin identified several phage display-selected peptides with apparent inhibition constants (K_i) in the micromolar range, among which was the tetrapeptide SWFP (K_i = 10.7 µ*M*; Skottrup *et al.*, 2012).

In order to understand the structural determinants of this inhibition, which would allow us to identify hit compounds for the development of drugs against Kly18, we determined the high-resolution X-ray crystal structure of the Kly18–SWFP complex. The results pave the way for the design of novel therapeutic strategies to palliate the effects of periodontal disease.

2. Materials and methods

2.1. Crystallization

Kly18 was prepared as reported by Karim *et al.* (2010). The complex between Kly18 and the SWFP peptide (Skottrup *et al.*, 2012) was obtained by mixing them in a 1:2 (enzyme:inhibitor) molar ratio (protein at 8.0 mg ml^{-1} and peptide at 5.3 mg ml^{-1}, both in buffer consisting of 5 m*M* Tris–HCl, 5 m*M* calcium chloride) and incubating the mixture at room temperature for 1 h. Crystallization assays were performed by the sitting-drop vapour-diffusion method. Reservoir solutions were prepared using a Tecan robot and 100 nl crystallization drops were dispensed onto 96 × 2-well MRC plates (Innovadyne) by a Phoenix nanodrop robot (Art Robbins) at the

Figure 1
The complex between Kly18 and the SWFP tetrapeptide. (*a*) Ribbon-type plot in cross-eyed stereo of Kly18 in the standard MP orientation (Gomis-Rüth *et al.*, 2012) showing the regular secondary-structure elements (α-helices as ribbons labelled αA–αC and β-strands as arrows labelled βI–βV). The segment delimiting the S_1' pocket is shown with its constituent parts in blue (Met-turn), orange (S_1' wall-forming segment) and yellow (specificity loop). Residues participating in the binding of the two zinc ions (magenta spheres) are shown with their side chains as tan C atoms and are labelled. The tetrapeptide is shown as a stick model with pink C atoms. The tentative potassium cation is displayed as a purple sphere. (*b*) Initial OMIT ($2F_{obs} - F_{calc}$)-type electron density in cross-eyed stereo contoured at 0.8σ above the threshold and centred on the final refined model of the inhibitory tetrapeptide (*Ser1-Trp2-Phe3-Pro4*). (*c*) Close-up view of (*a*) in cross-eyed stereo centred on the active-site cleft. Protein residues participating in delimiting the specificity pocket are shown as sticks with tan C atoms and are labelled if not labelled in (*a*). Solvent molecules are shown as cyan spheres. The side chain of Leu115 is in a double conformation. (*d*) Superposition in cross-eyed stereo of Kly18 in the present complex (protein in tan, inhibitor in pink) and in the serendipitous product complexes of its previously described magnesium-depleted (PDB entry 2xs3; protein in pale green, peptide in dark green) and magnesium-bound (PDB entry 2xs4; protein in pale blue, peptide in dark blue) forms (Cerdà-Costa *et al.*, 2011). The view is similar to that in (*c*). The cations correspond to those of the SWFP complex.

Table 1
Data-collection and processing statistics.

Values in parentheses are for the outermost resolution shell.

Synchrotron	ESRF
Beamline	ID14-4
Detector	ADSC Q315R
Data-collection date	31 July 2012
No. of frames	180
Exposure time (s)	1
Rotation increment (°)	1
Refined crystal-to-detector distance (mm)	239.4
Crystal mosaicity (°)	0.424
Space group	*I*4
Unit-cell parameters (Å)	a = 86.05, c = 49.44
Wavelength (Å)	0.9393
No. of measurements/unique reflections	183548/26344
Resolution range (Å)	42.9–1.55 (1.59–1.55)
Completeness (%)	99.9 (98.7)
$R_{\rm merge}$†	0.081 (0.749)
$R_{\rm r.i.m.}$ (= $R_{\rm meas}$)†	0.088 (0.854)
$\langle I/\sigma(I)\rangle$	18.4 (2.1)
Wilson B factor (Å^2)	21.2
Average multiplicity	7.0 (4.3)

† $R_{\rm merge} = \sum_{hkl}\sum_i |I_i(hkl) - \langle I(hkl)\rangle| / \sum_{hkl}\sum_i I_i(hkl)$; $R_{\rm r.i.m.} = \sum_{hkl}\{N(hkl)/[N(hkl)-1]\}^{1/2}\sum_i |I_i(hkl) - \langle I(hkl)\rangle| / \sum_{hkl}\sum_i I_i(hkl)$, where $I_i(hkl)$ is the ith intensity measurement and n_{hkl} is the redundancy of reflection hkl, including symmetry-related reflections, and $\langle I(hkl)\rangle$ is its average intensity. $R_{\rm r.i.m.}$, the redundancy-independent merging R factor (also known as $R_{\rm meas}$), is an improved multiplicity-weighted indicator of the quality of the data. For details, see Weiss (2001) and Evans (2006).

Table 2
Structure-refinement and validation statistics.

Resolution range used for refinement (Å)	∞–1.55
No. of reflections in working set/test set	24983/1335
Crystallographic R factor/free R factor†	0.145/0.171
No. of protein atoms‡	1311
No. of peptide atoms	39
No. of solvent molecules	208
No. of ligands	4 $(CH_2OH)_2CHOH$
No. of ions	2 Zn^{2+}, 1 K^+, 1 Na^+
R.m.s.d. from target values	
Bond lengths (Å)	0.010
Bond angles (°)	0.92
Overall average B factor (Å^2)	17.6
Model validation§	
Main-chain conformational angle analysis	
Residues in favoured regions	156 (97.5%)
Outliers	0
All residues	160
Poor rotamers (%)	0.72
Residues with bad bonds	0
Residues with bad angles	0
C^β deviations > 0.25 Å	0

† Crystallographic R factor = $\sum_{hkl}||F_{\rm obs}| - k|F_{\rm calc}||/\sum_{hkl}|F_{\rm obs}|$, where k is a scaling factor and $F_{\rm obs}$ and $F_{\rm calc}$ are the observed and calculated structure-factor amplitudes, respectively. This factor is calculated for the working-set reflections; the free R factor is calculated in the same way for a test set of reflections (>500) not used during refinement. ‡ Including atoms with double occupancy. § According to *MolProbity* (Chen *et al.*, 2010).

High-Throughput Crystallography Platform (PAC) at Barcelona Science Park. Plates were stored in Bruker steady-temperature crystal farms at 277 and 293 K. Successful conditions were scaled up to the microlitre range in 24-well Cryschem crystallization dishes (Hampton Research). The best crystals were obtained at 293 K from 1:1 µl drops of complex solution (8 mg ml^{-1} in 5 m*M* Tris–HCl pH 8, 5 m*M* calcium chloride, 0.02% sodium azide) with 0.4 *M* sodium/potassium tartrate as the reservoir solution. Crystals were cryoprotected by immersion into cryosolution [0.32 *M* sodium/potassium tartrate, 25%(*v*/*v*) glycerol].

2.2. Diffraction data collection

A complete diffraction data set was collected at 100 K from a liquid-nitrogen flash-cryocooled crystal (Oxford Cryosystems 700 Series Cryostream) using an ADSC Q315R CCD detector on beamline ID14-4 of the European Synchrotron Radiation Facility (ESRF, Grenoble, France) within the Block Allocation Group 'BAG Barcelona'. This crystal was body-centred tetragonal, with one complex per asymmetric unit, and was isomorphous to the previously reported magnesium-liganded form of Kly18 (Cerdà-Costa *et al.*, 2011). Diffraction data to 1.55 Å resolution were integrated, scaled, merged and reduced with the programs *XDS* and *XSCALE* (Kabsch, 2010; see Table 1).

2.3. Structure determination

The structure of the Kly18–SWFP complex (Fig. 1*a*) was solved by Fourier synthesis using the coordinates of the protein part only of the magnesium-liganded structure (PDB entry 2xs4; Cerdà-Costa *et al.*, 2011). Initial crystallographic refinement with the program *BUSTER*/*TNT* (Blanc *et al.*, 2004), which included TLS refinement, yielded an electron-density map that readily revealed that the inhibitor was anchored to the active-site cleft of the enzyme (Fig. 1*b*). Subsequent cycles of model building with *Coot* (Emsley *et al.*, 2010) were alternated with crystallographic refinement with *BUSTER*/*TNT* until completion of the model. The final model contained residues Tyr35–Asn53 and Leu58–Phe200 (protein residue numbering from UniProt sequence database entry D0EM77), four cations (two zinc, one potassium and one sodium, which replaces a solvent molecule found in the previous magnesium-bound structure), four glycerol molecules and 208 solvent molecules (see Table 2). Only the loop connecting strand βI to helix αA (Lβ1α1A; for the nomenclature and the extent of the regular secondary-structure elements, see Figs. 1*a* and 2*c* in Cerdà-Costa *et al.*, 2011) was partially disordered and was not traced for Ser54–His57.

2.4. Miscellaneous

Figures were prepared with *CHIMERA* (Pettersen *et al.*, 2004). Model validation was performed with *MolProbity* (Chen *et al.*, 2010) and the *WHATCHECK* routine of *WHAT IF* (Vriend, 1990). The final coordinates of the complex between *T. forsythia* Kly18 and the SWFP tetrapeptide have been deposited in the PDB (http://www.pdb.org) as entry 4in9. The apparent inhibition constant (K_i) of the peptide AFTS against Kly18 was determined as described by Skottrup *et al.* (2012).

3. Results and discussion

3.1. Structure of Kly18

The successful crystallization of Kly18–SWFP complex previously formed in solution only occurred under conditions containing sodium/potassium tartrate; these conditions were thus unrelated to those employed to obtain the magnesium-unbound and magnesium-bound forms (Cerdà-Costa *et al.*, 2011). The latter crystallized using 45% 2-methyl-2,4-pentanediol, 0.2 *M* ammonium acetate, 0.1 *M* Tris–HCl pH 8.5 and 14% sodium polyacrylate 5100, 20 m*M* magnesium chloride, 0.1 *M* HEPES pH 7.5, respectively, as reservoir solutions. The present crystals, however, were isomorphous to the magnesium-bound form and belonged to the tetragonal space group *I*4 (compare Table 1 with Table 2 of Cerdà-Costa *et al.*, 2011).

The structure of Kly18 conforms to the overall fold of MMPs (Tallant *et al.*, 2010) as described previously (Cerdà-Costa *et al.*, 2011). Briefly, it has a compact globular shape (Fig. 1*a*) traversed by a

shallow active-site cleft with a catalytic zinc ion at its bottom at half cleft-width. The former separates an upper N-terminal subdomain (NTS) from a lower C-terminal subdomain (CTS). The NTS consists of a twisted five-stranded β-sheet (strands βI–βV), two α-helices (the 'backing helix' αA and the 'active-site helix' αB) and an 'S-loop' (LβIIIβIV), which encompasses the binding site for a second structural zinc ion. The CTS contains the 'Met-turn', centred on Met173, which creates a hydrophobic pillow for the catalytic metal-binding site and is essential for the integrity of the site in MMPs and other members of the metzincin clan of MPs (Tallant *et al.*, 2010). In addition, the 'C-terminal helix' αC and a second structural cation-binding site, which is most likely to contain a potassium ion owing to geometric considerations (Harding, 2002) and its abundance in the crystallization conditions, are found in the CTS. The possible potassium is liganded in a distorted hexagonal coordination by six O atoms (2.7–3.0 Å apart) provided by the main-chain carbonyls of Ser75, Ser78 and Leu80 and by three solvent molecules.

As in MMPs in general, the catalytic zinc ion is bound by three histidines (here His155, His159 and His165) contained in a long consensus sequence characteristic to metzincins, HE*XX*H*XX*G*XX*H, which also contains the general base/acid glutamate, Glu156, required for catalysis (Tallant *et al.*, 2010). The top of the active-site cleft is shaped on its nonprimed side (for cleft-site nomenclature, see Gomis-Rüth *et al.*, 2012; Schechter & Berger, 1967) by the 'upper-rim strand' βIV of the NTS β-sheet and on its primed side by the final stretch of the S-loop, termed the 'bulge-edge segment'. The bottom of the active-site cleft on its primed side is in turn delimited by the segment bridging the Met turn and helix αC, which includes the 'S_1' wall-forming segment' (Pro175–Tyr177) at the front and the 'specificity loop' (Gly179–Gln183) at the back (Fig. 1*a*). Together with the first turn of the active-site helix αB, the latter three structural elements contribute to shaping the size and the chemical nature of the S_1' (or specificity) pocket in Kly18 and also in MMPs in general (Tallant *et al.*, 2010).

3.2. Inhibitor binding

The structure revealed the unambiguous presence of the tetrapeptide (*Ser1-Trp2-Phe3-Pro4*; peptide residues are shown in italics) in the initial (OMIT) electron-density maps (Fig. 1*b*). It is firmly anchored in a substrate-like manner to the primed side of the cleft, with the N-terminal α-amino group of *Ser1* bound to the catalytic zinc (at a distance of 2.2 Å), the $O^{\varepsilon2}$ atom of Glu156 (2.9 Å) and a solvent molecule (2.9 Å). The latter is itself further anchored to Glu156 $O^{\varepsilon1}$ (3.0 Å) and a second solvent molecule (2.7 Å; Fig. 1*c*). These two solvent molecules possibly mimic authentic substrate-atom positions on the nonprimed side of the cleft in Michaelis complexes. The overall arrangement of the inhibitor N-terminus strongly suggests that *Ser1* N is in its uncharged NH_2 protonation state, while Glu156 is possibly present as an anionic carboxylate. In contrast to true peptidic substrates in Michaelis complexes, none of the peptide main-chain atoms contact the protein main chain directly, with the only exception being *Phe3* N, which forms a hydrogen bond to Pro175 O of the S_1' wall-forming segment (at a distance of 2.8 Å).

Considering the peptide side chains, *Ser1* points away from the protein moiety into bulk solvent and is in van der Waals contact with the zinc-binding His165 (*Ser1* $O^{\gamma}\cdots$His165 $C^{\varepsilon1}$, 3.1 Å). The bulky aromatic side chain of *Trp2* penetrates the S_1' pocket of the enzyme, which is lined by the side chains of Leu73, Ile114–Leu115, Val152, His155, His165, Leu172–Tyr177 and Lys181–Arg182 (Fig. 1*c*). However, the presence of six solvent molecules at the bottom of the pocket indicates that the indole side chain far from fills it completely. In addition, Lys181 from the specificity loop closes the bottom of the pocket and is kept in place by a double hydrogen bond to the main-chain O atoms of the segment preceding the Met-turn (Lys181 $N^{\zeta}\cdots$ Ser169 O and Lys181 $N^{\zeta}\cdots$Ala171 O; both 2.9 Å). The positive charge of the lysine ε-amino group is not compensated by any protein residue. Downstream of *Trp2*, *Phe3* again points away from the cleft, but its side chain resides on a hydrophobic base which gives rise to the cleft subsite S_2' and is created by the side chains of the zinc-binding His165 and the S_1' wall residues Pro175 and Tyr177. After *Phe3*, the inhibitor peptide chain leaves the molecular surface of Kly18, so that *Pro4*, which is not so well defined by electron density (Fig. 1*b*), projects into the bulk solvent.

3.3. Comparison with previous Kly18 structures

Overall, the structure of SWFP-inhibited Kly18 is very similar to the previously reported structures of its magnesium-unbound (PDB entry 2xs3) and magnesium-bound (PDB entry 2xs4) variants (Fig. 1*d*; Cerdà-Costa *et al.*, 2011). In these structures, which were determined to resolutions of 2.40 and 1.70 Å, respectively, we had serendipitously trapped short peptides, which were probably C-terminal cleavage products resulting from the purification procedure, of four and three residues, respectively, on the primed side of the cleft, which were tentatively interpreted as AFT(S). Interestingly, we could not detect any inhibitory activity of the tetrapeptide AFTS towards Kly18 even at 0.125 m*M*. Superposition of the three structures reveals that they coincide overall except for the disorder found in LβIαA in the present complex and in the bulge-edge segment spanning Asp109–Ile114 (Fig. 1*d*). In the magnesium-unbound form this segment is completely folded out towards downstream primed positions of the cleft when compared with the other two structures, resulting in a maximal displacement of ∼12 Å for Thr112 C^{α} between the magnesium-unbound structure and the present complex structure. This suggests that the bulge-edge segment is flexible and is capable of adopting several conformations without affecting substrate, product or inhibitor binding, at least with respect to short peptides covering positions up to P_3'.

In addition, a magnesium ion is found in the magnesium-bound form of Kly18 coordinated by an octahedral-minus-one ligand sphere, with the apical position that points towards bulk solvent being unoccupied, close to the position of the structural potassium of the SWFP complex and with similar ligands (except for Leu80 O) but much shorter binding distances (2.1–2.5 Å). Overall, the polypeptide chain traces (Ser75–Ser81) coincide not only in the two ion-bound structures but also in the ion-depleted structures, suggesting that there is no evident structural explanation for the requirement of calcium for activity or ion binding in this region in general (Karim *et al.*, 2010; Cerdà-Costa *et al.*, 2011).

The overall structural similarity of the Kly18 complexes extends to the binding mode of the peptides to the active-site cleft (Fig. 1*d*), in particular for their side chains, thus supporting the structural conclusions derived from the present inhibitory-peptide complex structure. In particular, the preference of Kly18 for bulky hydrophobic residues in the P_1' position of substrates, as determined by applying the CLiPS methodology (Karim *et al.*, 2010), is met by *Trp2* in the present structure and by a phenylalanine in the other two structures.

4. Conclusion

We conclude that the inhibitory tetrapeptide SWFP binds to Kly18 in a very similar manner to the products left behind in the primed side of

the active-site cleft after cleavage of substrates. Both the presence of solvent molecules in the specificity pocket below the indole side chain of *Trp2* and the unbalanced positive charge of the pocket-bottom residue Lys181 strongly suggest that a chemically modified side chain that is bulky and hydrophobic at the peptide-proximal end but that is provided with a negatively charged group ∼8.6 Å from the position of the *Trp2* C^{α} atom could yield a much stronger and specific inhibitor of Kly18 than SWFP. In addition, the lack of contact of *Pro4* with the protein moiety suggests that substrate-subsite positions beyond P_3' are probably not relevant for the design of specific active-site inhibitors of Kly18. Further experiments will be required to verify these points and could pave the way to the design of small-molecule inhibitors that may assist in the development of novel drugs to combat *Tannerella* infection.

We are grateful to the Automated Crystallography Platform at IBMB/IRB/PCB for assistance during crystallization experiments. We acknowledge the help provided by local contacts at the ESRF synchrotron. Funding for data collection was provided in part by the ESRF. This study was supported in part by grants from European, American, Polish, Spanish, Danish and Catalan agencies (2012/04/A/NZ1/00051, 2011/03/N/NZ1/00586, 2137/7.PR-EU/2011/2, DE09761, FP7-HEALTH-F3-2009-223101 'AntiPathoGN', FP7-HEALTH-2010-261460 'Gums&Joints', FP7-PEOPLE-2011-ITN-290246 'RAPID', BIO2009-10334, BFU2012-32862, CSD2006-00015, Lundbeck Foundation grant R54-A5291 and Fundació 'La Marató de TV3' grants 2009-100732 and 2009SGR1036). The Faculty of Biochemistry, Biophysics and Biotechnology of the Jagiellonian University in Kraków (Poland) is a beneficiary of structural funds from the European Union (grant No POIG.02.01.00-12-064/08 'Molecular Biotechnology for Health'). The funders had no role in the study design, data collection and analysis, decision to publish or preparation of this manuscript.

References

Blanc, E., Roversi, P., Vonrhein, C., Flensburg, C., Lea, S. M. & Bricogne, G. (2004). *Acta Cryst.* D**60**, 2210–2221.
Cerdà-Costa, N., Guevara, T., Karim, A. Y., Ksiazek, M., Nguyen, K. A., Arolas, J. L., Potempa, J. & Gomis-Rüth, F. X. (2011). *Mol. Microbiol.* **79**, 119–132.
Chen, V. B., Arendall, W. B., Headd, J. J., Keedy, D. A., Immormino, R. M., Kapral, G. J., Murray, L. W., Richardson, J. S. & Richardson, D. C. (2010). *Acta Cryst.* D**66**, 12–21.
Emsley, P., Lohkamp, B., Scott, W. G. & Cowtan, K. (2010). *Acta Cryst.* D**66**, 486–501.
Evans, P. (2006). *Acta Cryst.* D**62**, 72–82.
Gomis-Rüth, F. X. (2003). *Mol. Biotechnol.* **24**, 157–202.
Gomis-Rüth, F. X. (2009). *J. Biol. Chem.* **284**, 15353–15357.
Gomis-Rüth, F. X., Botelho, T. O. & Bode, W. (2012). *Biochim. Biophys. Acta*, **1824**, 157–163.
Harding, M. M. (2002). *Acta Cryst.* D**58**, 872–874.
Jusko, M., Potempa, J., Karim, A. Y., Ksiazek, M., Riesbeck, K., Garred, P., Eick, S. & Blom, A. M. (2012). *J. Immunol.* **188**, 2338–2349.
Kabsch, W. (2010). *Acta Cryst.* D**66**, 133–144.
Karim, A. Y., Kulczycka, M., Kantyka, T., Dubin, G., Jabaiah, A., Daugherty, P. S., Thogersen, I. B., Enghild, J. J., Nguyen, K. A. & Potempa, J. (2010). *Biol. Chem.* **391**, 105–117.
Koziel, J., Karim, A. Y., Przybyszewska, K., Ksiazek, M., Rapala-Kozik, M., Nguyen, K.-A. & Potempa, J. (2010). *J. Innate Immun.* **2**, 288–293.
Petersen, P. E. & Ogawa, H. (2005). *J. Periodontol.* **76**, 2187–2193.
Pettersen, E. F., Goddard, T. D., Huang, C. C., Couch, G. S., Greenblatt, D. M., Meng, E. C. & Ferrin, T. E. (2004). *J. Comput. Chem.* **25**, 1605–1612.
Pomerantsev, A. P., Pomerantseva, O. M., Moayeri, M., Fattah, R., Tallant, C. & Leppla, S. H. (2011). *Protein Expr. Purif.* **80**, 80–90.
Rôças, I. N., Siqueira, J. F. Jr, Santos, K. R. N. & Coelho, A. M. A. (2001). *Oral Surg. Oral Med. Oral Pathol. Oral Radiol. Endod.* **91**, 468–471.
Schechter, I. & Berger, A. (1967). *Biochem. Biophys. Res. Commun.* **27**, 157–162.
Sharma, A. (2010). *Periodontol. 2000*, **54**, 106–116.
Skottrup, P. D., Sorensen, G., Ksiazek, M., Potempa, J. & Riise, E. (2012). *PLoS One*, **7**, e48537.
Socransky, S. S., Haffajee, A. D., Cugini, M. A., Smith, C. & Kent, R. L. Jr (1998). *J. Clin. Periodontol.* **25**, 134–144.
Tallant, C., Marrero, A. & Gomis-Rüth, F. X. (2010). *Biochim. Biophys. Acta*, **1803**, 20–28.
Vriend, G. (1990). *J. Mol. Graph.* **8**, 52–56.
Weiss, M. S. (2001). *J. Appl. Cryst.* **34**, 130–135.